Neuron
Article

Motor Behavior Activates Bergmann Glial Networks

Axel Nimmerjahn,[1,*] Eran A. Mukamel,[1] and Mark J. Schnitzer[1,2,*]
[1]James H. Clark Center for Biomedical Engineering & Sciences
[2]Howard Hughes Medical Institute
Stanford University, 318 Campus Drive West, Stanford, CA 94305, USA
*Correspondence: animmerj@stanford.edu (A.N.), mschnitz@stanford.edu (M.J.S.)
DOI 10.1016/j.neuron.2009.03.019

SUMMARY

Although it is firmly established that neuronal activity is a prime determinant of animal behavior, relationships between astrocytic excitation and animal behavior have remained opaque. Cerebellar Bergmann glia are radial astrocytes that are implicated in motor behavior and exhibit Ca^{2+} excitation. However, Ca^{2+} excitation in these cells has not previously been studied in behaving animals. Using two-photon microscopy we found that Bergmann glia exhibit three forms of Ca^{2+} excitation in awake, behaving mice. Two of these are ongoing within the cerebellar vermis. During locomotor performance concerted Ca^{2+} excitation arises in networks of at least hundreds of Bergmann glia extending across several hundred microns or more. Concerted Ca^{2+} excitation was abolished by anesthesia or blockade of either neural activity or glutamatergic transmission. Thus, large networks of Bergmann glia can be activated by specific animal behaviors and undergo excitation of sufficient magnitude to potentially initiate macroscopic changes in brain dynamics or blood flow.

INTRODUCTION

Neurons have long been studied in live animals by electrophysiological techniques, but astrocytes' lack of electrical excitability has made these cells' relationships to animal behavior more challenging to uncover. Nonetheless, since the discovery of astrocytic Ca^{2+} excitation in vitro, multiple processes that involve astrocytic Ca^{2+} signaling have emerged. In adults these include modulation of neuronal activity and regulation of cerebral blood flow (Fiacco and McCarthy, 2006; Iadecola and Nedergaard, 2007). However, the current in vivo data generally share two limitations.

First, results have generally been obtained in anesthetized animals, and with the exception of one paper that noted Ca^{2+} transients in neocortical astrocytes in behaving mice (Dombeck et al., 2007), it is largely unexplored whether there are specific behaviors that elicit astrocytic Ca^{2+} excitation. Anesthesia precludes animal behavior, and neuronal dynamics can be quite distinct in the anesthetized and awake brain (Greenberg et al., 2008; Rinberg et al., 2006). Since astrocytic dynamics may reflect aspects of neuronal activity (Fiacco and McCarthy, 2006), the strong possibility exists that astrocytes will show equally divergent dynamics across brain states.

A second issue is that in vivo studies to date have mainly examined neocortical protoplasmic astrocytes. Like neurons, astrocytes display considerable nonuniformity, so astrocytic dynamics might vary substantially between brain areas and layers (Fiacco and McCarthy, 2006; Takata and Hirase, 2008). In the adult brain, a basic distinction exists between the radial astrocytes, which include the Bergmann glia of the cerebellar cortex and Müller cells of the retina, and the protoplasmic "star-shaped" astrocytes of the neocortex and other areas. These two classes exhibit markedly different morphologies and in vitro patterns of Ca^{2+} excitation (Fiacco and McCarthy, 2006). Thus, the patterns of Ca^{2+} excitation seen in protoplasmic astrocytes and Bergmann glia of behaving animals may be expected to differ substantially.

Motivated both by the recent imaging progress and the above limitations, we studied Ca^{2+} excitation within Bergmann glial networks in awake, behaving mice. We focused on a basic behavior, locomotion, to ascertain whether Bergmann glia have behaviorally triggered dynamics. These cells lie in areas crucial for motor coordination, are implicated in motor behavior (Shibuki et al., 1996), form gap-junction-coupled networks, and can be identified by the palisade arrangement of their fibers and status as the sole astrocytes in the cerebellar molecular and Purkinje cell layers. We developed methods for two-photon imaging in the cerebellum of awake, head-restrained mice allowed to move on an exercise ball and studied how wakefulness and motor behavior affect Ca^{2+} excitation as it normally occurs in Bergmann glial networks.

We found that Bergmann glia of the cerebellar vermis, an area implicated in locomotor coordination, exhibit three forms of Ca^{2+} transients in awake mice. One of these, which we named "Ca^{2+} flares," was triggered during locomotion and extended over macroscopic domains at least hundreds of microns across. Flares involved large networks of astrocytes, with at minimum hundreds of Bergmann glial fibers, and arose with onset kinetics similar to those of local increases in blood perfusion accompanying locomotion. The other two forms of Ca^{2+} excitation, which we named "sparkles" and "bursts," were ongoing in awake, resting animals. Sparkles appeared to be restricted to individual fibers. Bursts were radial waves expanding in three dimensions across the fibers of ~10–40 Bergmann glia. The dependence of flares on locomotion and the absence of flares and near abolition of sparkles under anesthesia emphasize that studies in awake animals are essential.

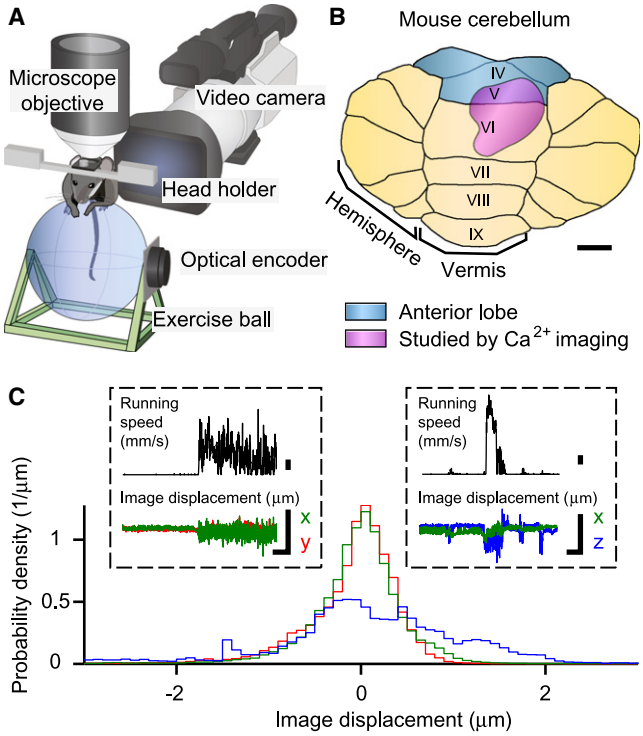

Figure 1. Two-Photon Microscopy in Cerebellar Cortex of Behaving Mice

(A) Two-photon microscopy in awake, head-restrained mice using an exercise ball. Mouse locomotion was tracked by an optical encoder on the ball, which provided a sensitive, quantitative, and repeatable readout of running onset/offset, speed, and direction. In addition, mouse behavior was recorded on video (Supplemental Data).

(B) Areas of lobules V and VI of the cerebellar vermis examined in this study by Ca^{2+} imaging (pink). Scale bar: 1 mm.

(C) Probability densities of image displacements in dorso-ventral (z, blue), medio-lateral (x, green) and rostro-caudal (y, red), dimensions from a set of seven example experiments. (Insets) Colored traces show x (green) and y (red) image displacements (left inset), or x (green) and z (blue) image displacements (right inset), during two examples of mouse locomotion (black trace). x and y displacements were corrected by image registration prior to data analysis. Scale bars: upper, 50 mm/s; lower, 10 s and 5 μm.

RESULTS

Imaging Bergmann Glia in Awake Mice during Rest and Locomotion

Our first goal was to visualize glial Ca^{2+} transients in behaving mice without undue levels of motion artifact. To achieve this we used two-photon microscopy in awake, head-restrained mice allowed to run voluntarily on an exercise ball that rotates about one axis (Figure 1). We monitored rotation of the exercise ball using an optical encoder that reports rotations as slight as 0.5°, corresponding to 0.5 mm movements along the running surface (Figure 1A). This provides a sensitive measure of locomotion that does not rely on electromyography, which can suffer from crosstalk between muscles in mice (Koekkoek et al., 2002).

After habituating a mouse to periods of head restraint, we created an optical window in the cranium, injected the membrane-permeant fluorescent Ca^{2+} indicator Oregon-Green-488-BAPTA-1-acetoxymethyl (OGB-1-AM) into cerebellar cortex, and performed Ca^{2+} imaging across areas 200–500 μm wide with the cranium held secure. With this approach we studied lobules V and VI of the vermis (Figure 1B), areas implicated in coordinating hindlimbs and forelimbs (Andersson and Armstrong, 1987; Leicht and Schmidt, 1977), particularly the ipsilateral forelimb in rodent (Jorntell et al., 2000).

Within OGB-1-AM fluorescence images Bergmann glia could be identified by the distinct palisade arrangement of their fibers in the molecular layer, and the size and location of their somata in the Purkinje cell layer (De Blas, 1984; Reichenbach et al., 1995) (Figure 2). However, since OGB-1-AM also labels neurons, we sought a way to identify Bergmann glia more readily by using an established astrocyte marker of a different color, the red fluorescent dye sulforhodamine 101 (SR101) (Nimmerjahn et al., 2004). To confirm that SR101 marks Bergmann glia, we applied SR101 to the cerebellar cortex of S100β-EGFP Kosmos mice, which express green fluorescent protein (GFP) in astrocytes under the control of the S100β promoter (Zuo et al., 2004). The spatial distributions of GFP expression and SR101 labeling were virtually identical, distinguishable only by their intensity variations (Figures 2A and S1, available online). SR101 stained Bergmann glial end-feet contacting blood vessels, glia limitans near the pia mater, rows of palisade fibers extending in the dorsal-ventral dimension, and densely packed somata surrounding Purkinje cell bodies (Figures S1 and S2). The root mean square radii that we estimated from both high-magnification SR101 images of palisade fibers in cross-section (0.95 ± 0.6 μm; n = 1374 palisade fibers, 10 mice) and SR101 images acquired at lower magnifications used for Ca^{2+} imaging (1.8 ± 0.6 μm; n = 15613 palisade fibers, 17 mice) were consistent with the prior estimate of ~1.5 μm radius for palisade fibers examined by electron microscopy (Grosche et al., 1999). Thus, as in prior studies of Ca^{2+} dynamics in neocortical astrocytes using OGB-1-AM and SR101 (Nimmerjahn et al., 2004), the SR101 counterstain allowed Bergmann glia to be identified unambiguously (Figure 2B and Movie S2, available online).

Since SR101 is a nonfunctional morphological marker, we also used it to characterize the motion artifacts in our imaging data from awake, behaving mice. When the mice were not driving the exercise ball, motion artifacts in both lateral (medio-lateral [x]: ± 0.4 μm SD; rostro-caudal [y]: ± 0.6 μm SD; n = 74 events, 3 mice) and axial (dorso-ventral [z], ± 1.5 μm SD; n = 19 events, 4 mice) dimensions were essentially negligible. During mouse locomotion there were small, transient in-plane displacements (x: ± 0.7 μm SD; y: ± 0.8 μm SD; n = 74 events, 3 mice; Figure 1C) that were correctible by offline image registration. Artifacts due to axial displacements (z: ± 3.4 μm SD; n = 19 events, 4 mice; Figure 1C) were largely mitigated by the coinciding alignments of the optical axis and Bergmann glial palisade fibers in the dorsal-ventral direction. Crucially, within SR101 images we saw no characteristic phenomena resembling the forms of Ca^{2+} excitation seen repeatedly in OGB-1-AM images, from all 33 alert mice studied.

Having achieved a suitable imaging assay, we next characterized these forms of Ca^{2+} excitation in detail. As elaborated below, all the Ca^{2+} transients we describe occurred within, but

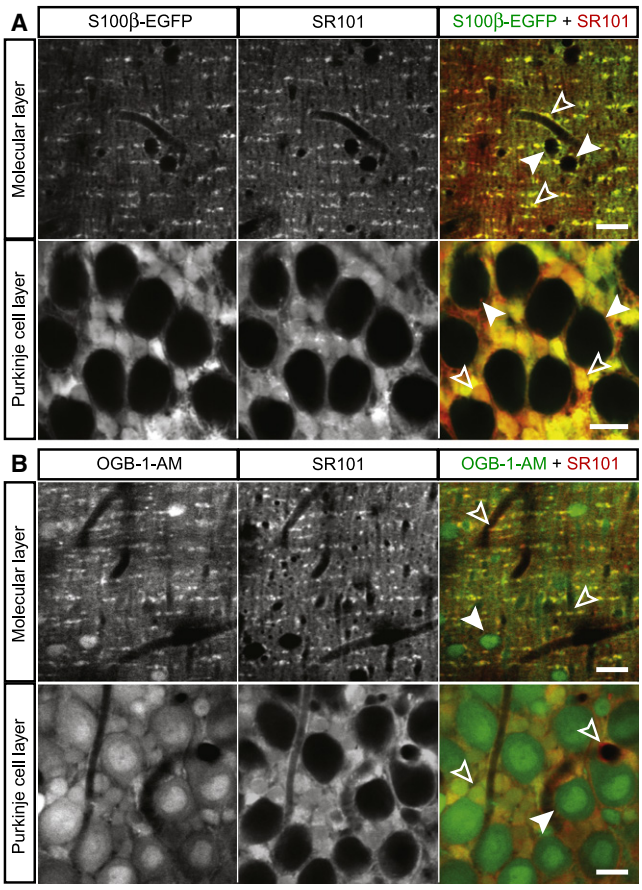

Figure 2. Palisades and Somata of Bergmann Glia Were Identified Based on Anatomical Features and Sulforhodamine 101 Costaining

(A) The red fluorescent astrocyte marker sulforhodamine 101 (SR101) stains Bergmann glia in the cerebellar cortex of adult mice. Localization of SR101 to Bergmann glia was verified in the Kosmos mouse line expressing EGFP under the control of an S100β promoter, an established marker of astrocytes. (Left) EGFP expression in Bergmann glia of the Kosmos line. (Center) SR101 staining pattern in the same mouse. (Right) Image overlays showing that SR101 stains Bergmann glia somata and palisade fibers (yellow, open arrow heads) in the Purkinje cell (bottom) and molecular layers (top), respectively. Molecular layer interneurons and Purkinje cells (closed arrow heads) are labeled neither in the Kosmos line nor by SR101.

(B) SR101 costaining was used to identify Bergmann glial palisades and somata in OGB-1-AM fluorescence images. (Left) OGB-1-AM staining pattern in the molecular (top) and Purkinje cell layer (bottom). (Center) SR101 staining in the same mouse. (Right) Overlay images, in which Bergmann glia fibers, end-foot processes, and somata are indicated (open arrow heads) (see also Figures S1 and S2). Molecular layer interneurons and Purkinje cells (closed arrow heads in top and bottom rows, respectively) are stained by OGB-1-AM, but not SR101.

Scale bars: 15 μm.

were not strictly limited to, image regions of interest (ROIs) demarcating SR101-labeled palisade fibers. These transients exhibited time courses that evolved on the seconds timescale, consistent with these occurring in nonneuronal cells lacking fast Ca^{2+} dynamics, and were quite distinct from the rapid dendritic Ca^{2+} spikes (~10 ms rise time) we regularly observed in Purkinje neurons.

Localized Ca^{2+} Sparkles are Ongoing in Awake Mice

When alert mice were on the exercise ball but voluntarily sitting still, we observed two forms of spontaneous Ca^{2+} excitation in Bergmann glial fibers. The first of these forms was markedly sensitive to isoflurane anesthesia, and we termed these events Ca^{2+} sparkles due to their highly localized appearance.

Sparkles occurred within individual palisade fiber ROIs (Figures 3A–3D), which had been identified by SR101 labeling and collectively exhibited arrangements and sizes consistent with those of Bergmann glial main fibers (Figures 2A and S1). At higher optical magnifications we saw that sparkles sometimes included regions surrounding the palisade fibers (Figure 3C). However, the resolution of our imaging data did not permit us to determine conclusively whether individual finer Bergmann glial processes, which are very dense outside the palisades and closely entwined with neuronal processes, also undergo Ca^{2+} excitation.

Sparkles were modest in amplitude, with relative fluorescence increases [$\Delta F(t)/F$] sometimes just above background fluctuations (see Table S1 [available online] for an overview of sparkle properties). To study sparkles' time evolution, we examined the subset of sparkles that passed a threshold criterion of having a >10% increase in $\Delta F(t)/F$. This approach is conservative, in that the selected events can be readily identified above background noise, but it does lead to an underestimate of event rates. Within this event subset [peak $\Delta F(t)/F$; 13.2% ± 4.1%, mean ± SD; range, 10.1%–134.3%; n = 4285 events, 15 mice], sparkles had variable duration (3.3 ± 3.9 s; range, 0.5–35.4 s; n = 4285 events, 15 mice) (Figures 3B and 3D). The estimated lower bound on the frequency of sparkles was 4.5 ± 2.6 Hz/mm^2 (range, 1.1–11.0 Hz/mm^2; n = 4285 events, 15 mice) (Figure 3B). By considering the density of glial fibers and the proportion of the molecular layer sampled in our recordings, we estimated that this bound corresponds to a mean rate of sparkles of ~0.01–0.1 min^{-1} per individual glial fiber. This is comparable to spontaneous Ca^{2+} excitation rates for neocortical astrocytes (Hirase et al., 2004; Takata and Hirase, 2008).

Sparkle rates were reduced but not abolished by local blockade of either neuronal activity using the Na^+ channel blocker tetrodotoxin (TTX) (1.5 ± 0.5 Hz/mm^2; range, 1.0–2.2 Hz/mm^2; likelihood ratio test, $p < 10^{-6}$; n = 277 events, 5 mice) or glutamatergic transmission using the broad-spectrum glutamate receptor antagonist γ-D-glutamylglycine (γDGG) (3.6 ± 2.3 Hz/mm^2; range, 0.5–5.7 Hz/mm^2; likelihood ratio test, $p < 0.002$; n = 614 events, 4 mice). Pyridoxalphosphate-6-azephenyl-2′,4′-disulfonic acid (PPADS), a nonselective P2 purinergic blocker, failed to reduce sparkle rates (5.7 ± 2.5 Hz/mm^2; range, 3.3–8.4 Hz/mm^2; likelihood ratio test, $p > 0.2$; n = 974 events, 3 mice). However, in mice anesthetized by isoflurane, sparkle rates fell markedly (0.2 ± 0.1 Hz/mm^2; range, 0.0–0.3 Hz/mm^2; likelihood ratio test, $p < 10^{-5}$; n = 14 events, 4 mice). In summary, as reported for other types of astrocytes (Nett et al., 2002; Takata and Hirase, 2008) there appears to be an "intrinsic" subpopulation of Ca^{2+} transients that persists under blockade of neuronal activity and another subpopulation that does not.

In contrast to the sparkles we regularly saw in palisade fibers, we only occasionally saw spontaneous Ca^{2+} transients in Bergmann glial somata. The latter events were almost three orders of

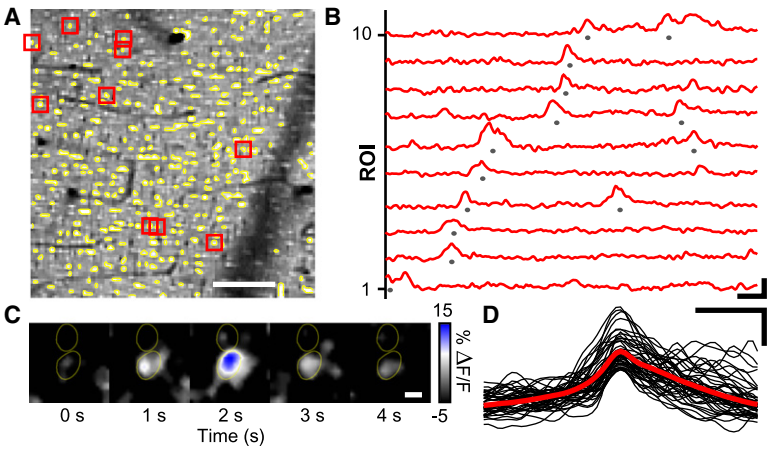

Figure 3. Sparkles Are Ongoing Ca^{2+} Transients that Appear in Individual Palisade Fibers

(A) OGB-1-AM image showing cellular structures in a superficial region of the cerebellar molecular layer. Ca^{2+} dynamics were analyzed in regions of interest (ROIs) where palisade fibers (yellow) had been identified by SR101 costaining. Example traces of relative increases in OGB-1-AM fluorescence, $\Delta F(t)/F$, from 10 ROIs marked red are shown in (B). Scale bar: 50 μm. (B) Traces of Ca^{2+} signals from individual palisade fiber ROIs show examples of sparkles, defined as events of >10% $\Delta F(t)/F$ (marked by gray dots) for purposes of analysis. Traces are arranged by sparkle onset time. Scale bars: 5 s, 10% $\Delta F(t)/F$. (C) High-magnification OGB-1-AM $\Delta F(t)/F$ images showing a Ca^{2+} sparkle in one out of two neighboring palisade fibers, whose perimeters (yellow outlines) were determined from the simultaneously acquired SR101 images. Scale bar: 3 μm. (D) Overlay of 45 individual sparkle time courses (black) and an averaged trace (red) for sparkles that occurred within the yellow ROIs in (A). Scale bars: 5 s, 10% $\Delta F(t)/F$.

magnitude less frequent (~8.9 ± 3.7 mHz/mm^2; n = 24 recordings, 14 mice), and involved large $\Delta F(t)/F$ increases (22% ± 12%; n = 12 events, 14 mice) that were localized to one or a few neighboring somata.

Ca^{2+} Bursts Involve up to ~40 Bergmann Glial Cells in Alert Mice

Like sparkles, bursts occurred spontaneously in mice resting voluntarily on the exercise ball. Bursts appeared as radially expanding waves that spread over approximately ellipsoidal regions with greater medio-lateral (55 ± 37 μm; n = 63, 9 mice; Wilcoxon signed rank test, $p < 0.001$) than rostro-caudal extent (44 ± 33 μm; n = 63, 9 mice; Wilcoxon signed rank test, $p < 0.001$) (Figure 4). These waves swept over both palisade regions, where the primary Bergmann glial fibers could clearly be seen in the movie data to undergo Ca^{2+} activation, and nonpalisade regions, where we could not resolve the individual fibers or anatomical processes involved. Peak $\Delta F(t)/F$ increases for bursts (12.9% ± 4.8 %; range, 2.8%–24.8%; n = 96 events, 11 mice) were similar to those for sparkles, but the two phenomena were unmistakably distinct since bursts occupied much larger volumes (Figure 4 and Movie S1). Like sparkles, bursts were infrequent, but rates varied substantially between mice (168 ± 187 mHz/mm^2; range, 36.7–566 mHz/mm^2; n = 161 events, 8 mice).

By using 3D two-photon imaging to monitor multiple tissue depths with near simultaneity (Gobel et al., 2007), we found that bursts originated across all depths of the molecular layer and had axial extents of 56 ± 23 μm (n = 10 events, 5 mice) centered around the point of initiation (Figures 4E and Movie S1). Typical burst volumes (86,000 ± 61,000 μm^3; n = 10 events, 5 mice) obtained by 3D imaging implicate the involvement of many fine fibers and several main fibers from several neighboring Bergmann glia. Based on these cells' somatic density and the projection pattern of their ~2–5 main fibers per cell (De Blas, 1984; Reichenbach et al., 1995), we estimate that a burst encompasses on average ~10 but up to ~36 Bergmann glia. However, after having characterized bursts' volumes, we used only 2D imaging for examination of bursts' temporal profiles, due to the superior time resolution (~12–20 Hz frame rate) of 2D as compared to 3D imaging (1–4 Hz).

We examined closely the time course of fluorescence rise and decline within bursts' central regions, where the signal was sufficiently high enough above background levels to permit detailed analysis. Bursts displayed time courses (Figure 4B) similar to the time evolution of Bergmann glial Ca^{2+} transients in vitro, as previously recorded from fixed locations within cerebellar slices in response to parallel fiber stimulation (Beierlein and Regehr, 2006; Piet and Jahr, 2007). The similarity suggests that both phenomena might involve ATP-triggered release of Ca^{2+} from intracellular stores, as found in vitro. Consistent with this, bursts were virtually eliminated by PPADS (1.5 ± 3.0 mHz/mm^2; n = 1 event, 4 mice; likelihood ratio test, $p < 0.01$). However, bursts persisted in vivo after application of TTX (41 ± 48 mHz/mm^2; n = 38 events; likelihood ratio test, $p > 0.01$ in 7 out of 8 mice), γDGG (28 ± 23 mHz/mm^2; n = 9 events; likelihood ratio test, $p > 0.1$ in 2 out of 4 mice), or isoflurane anesthesia (28 ± 50 mHz/mm^2; n = 23 events, 18 mice; likelihood ratio test, $p > 0.01$) (Table S2).

We found that the burst time course was well modeled kinetically by a simple biochemical cascade of two reaction events in sequence, $0 \xrightarrow{k_1} 1 \xrightarrow{k_2} 2$. k_1 and k_2 denote the rate constants for transitions out of an initial state of resting [Ca^{2+}] (state 0), and a transient state in which [Ca^{2+}] is elevated (state 1) (respectively). This reaction scheme leads to a time course that is the convolution of two exponentials, and bursts' time courses conformed closely to this mathematical form with $1/k_1$ = 1.5 ± 0.7 s and $1/k_2$ = 1.8 ± 1.2 s (r = 0.9 ± 0.1; n = 96 events, 11 mice). The two rate constants for each burst were highly correlated, with 81% of events showing a negligible (<1%) difference between $1/k_1$ and $1/k_2$, which suggests that both rate constants might depend on a common factor.

In the presence of γDGG, $1/k_1$ values (2.2 ± 1.2 s; range, 0.7–3.6 s; n = 7 events, 2 mice; Wilcoxon rank sum test, $p < 0.1$) did not change significantly. However, $1/k_2$ values increased (9.6 ± 10 s; range, 3.3–30 s; n = 7 events, 2 mice; Wilcoxon rank sum test, $p < 0.001$) as compared to all other pharmacological conditions (Figure 4B). Since bursts persist under γDGG, glutamate

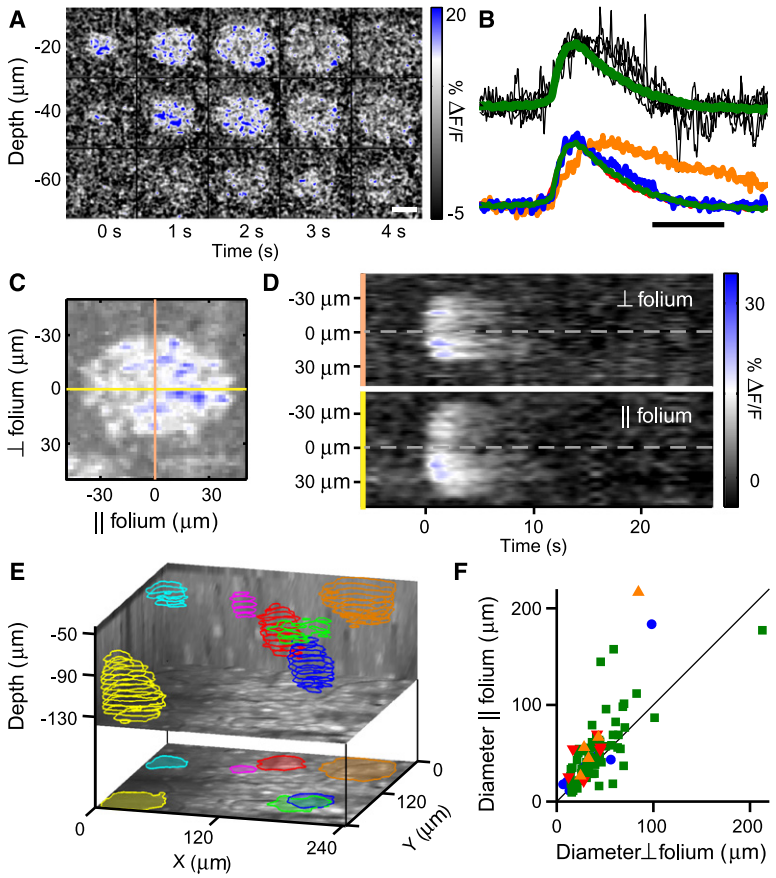

Figure 4. Bursts Are Ongoing Ca^{2+} Transients Spreading as 3D Radial Waves over Multiple Bergmann Glia

(A) Example 3D imaging data showing $\Delta F(t)/F$ optical cross-sections of OGB-1-AM fluorescence at five time points. Indicated depth values are relative to the pial surface. Scale bar: 50 μm.

(B) (Top) Six individual (black) $\Delta F(t)/F$ time traces for bursts and the mean time course (green) averaged over 96 bursts in 11 animals, measured over fixed areas that covered the bursts' centers in awake, resting mice. (Bottom) Averaged and normalized $\Delta F(t)/F$ traces under four conditions: isoflurane-anesthetized (blue; n = 8 events, 5 mice), awake and resting (green; n = 96 events, 11 mice), TTX-treated (red; n = 9 events, 5 mice), and γDGG-treated (orange; n = 7 events, 2 mice). Different animals were used for different drugs. Scale bar: 5 s.

(C) Cross-sectional $\Delta F(t)/F$ fluorescence image of a burst at a fixed depth and time. Yellow and peach lines indicate directions parallel and perpendicular to the cerebellar folium, respectively.

(D) $\Delta F(t)/F$ time courses along the yellow- and peach-colored lines in (C). Note that bursts have larger diameter in the direction parallel to the folium and spread outward from a central initiation site.

(E) (Top) Locations and volumetric profiles of seven bursts detected by 3D imaging during an 8.2 min period. Colored outlines show extent of Ca^{2+} spread for each burst at various depths. (Bottom) Z-projection image.

(F) Population data showing that bursts have greater extent parallel to the long axis of the cerebellar folium, which lies perpendicular to the parasagittal planes of cerebellar cortex. Colored data points denote individual bursts recorded under the four conditions noted in (B).

reception might play a role in bursts' termination, but perhaps not in their initiation (Discussion).

Given that bursts expand outward from a central initiation point, Ca^{2+} excitation might be initiated by the diffusion of a small molecule trigger, such as ATP. Since bursts only propagated over tens of microns, we could only estimate an approximate 3D diffusion constant (~150 $\mu m^2/s$; n = 13 events, 4 mice) and propagation speed (~10 μm/s; n = 11 events, 4 mice) (Supplemental Discussion).

Motor Behavior Activates Ca^{2+} Flares across Bergmann Glial Networks

When mice ran voluntarily on the exercise ball, concerted Ca^{2+} excitation arose in large networks of Bergmann glia in the vermis. These events, which we termed flares, occurred at the onset of locomotion and appeared to be composed of a large number of sparkles combined with Ca^{2+} excitation in areas surrounding the palisade fibers (Figure 5 and Movie S2). Flares often covered our entire field of view (200–500 μm) and thus typically involved the hundreds of Bergmann glial palisade fibers we could see, as well as adjoining areas between the palisades.

Because astrocytes have been reported to show Ca^{2+} responses to mechanical stress, we were initially concerned flares might be artifacts due to transient mechanical perturbation to the brain at running onset. However, multiple lines of evidence and control experiments were inconsistent with this possibility, leading us to conclude that flares are part of normal brain physiology. First, flares show a completely different time course (Figures 5 and 6) and are an order of magnitude more rapid than the Ca^{2+} signals reported to occur in response to mechanical stress (Charles et al., 1991; Chen et al., 1999). Second, flares occurred in our movie data even when there was no perceptible movement of the brain (Figure S4A). Third, in cases when there were measurable, micron-scale brain displacements at motor onset, we found no correlation between the magnitude of tissue displacements and either the occurrence or amplitude of Ca^{2+} flares (Figure S4B). Fourth, the occurrences of flares were independent of mechanical factors such as the craniotomy size (e.g., 3.0, 5.0, and 7.5 mm^2 for the recordings of Figures S4A and S3, and Figures 5A–5D, respectively), whether the dura mater was removed, or whether the craniotomy was covered with agarose and a coverslip. Fifth, we never saw flares in control experiments with awake mice in which we applied pressure on the animal's head holder or optical window (n = 30 stimulations, 3 mice; Figure S3). This was so even when the applied pressure caused far greater tissue displacements than those occurring during running-evoked flares in the same mice. Sixth, there were many instances of substantial brain displacements when the mice were not running and these did not produce flares (Figure S4B). Seventh, flares were abolished by blockade of neuronal Na^+ channels or glutamatergic transmission (Figure 6), showing that flares require neuronal activity and do not arise from direct mechanical activation of individual Bergmann glia. Eighth, we saw during flares no signs of spreading neuronal depression, a known effect of mechanical injury to the brain

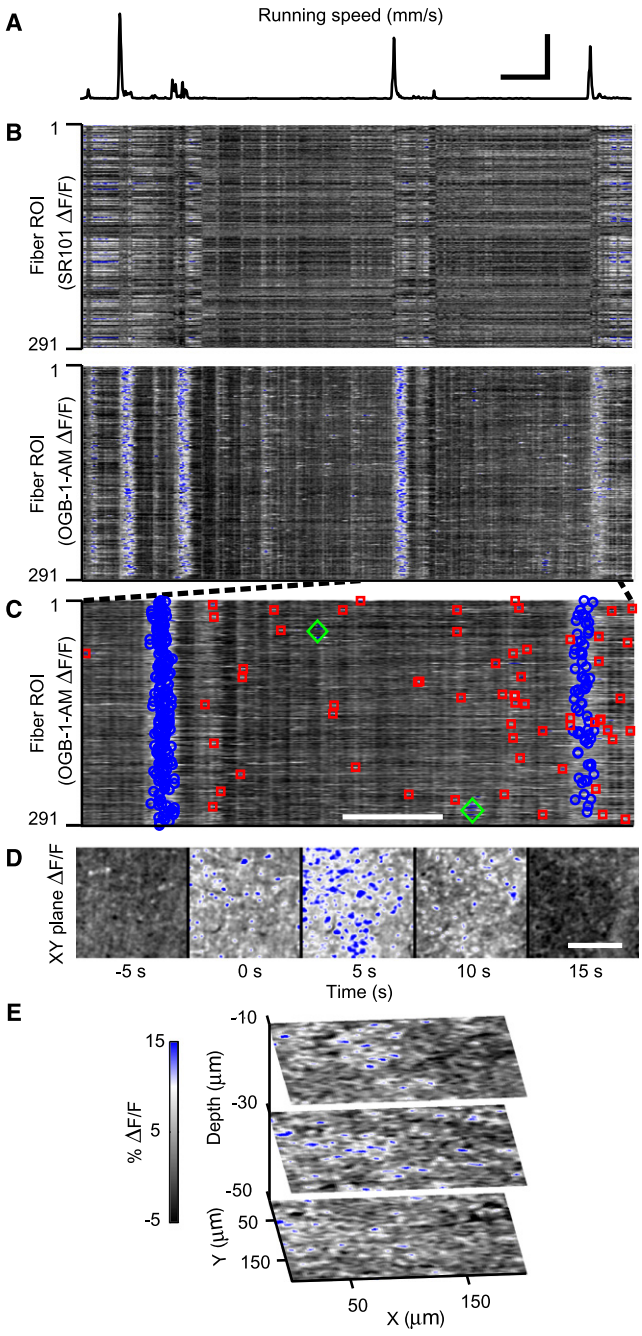

Figure 5. Motor Behavior Evokes Concerted Ca^{2+} Excitation across Bergmann Glial Networks

(A) Encoder trace of the exercise ball's rotational speed, showing multiple running bouts during an example 9.8 min period. Scale bars: 50 s and 20 mm/s; the former also applies to (B). (B) (Top) SR101 $\Delta F(t)/F$ traces from 291 palisade fiber ROIs during the same time interval as in (A). (Bottom) The same palisade fiber ROIs in OGB-1-AM images reliably exhibit concerted $\Delta F(t)/F$ increases, flares, during running. Signals of similar magnitude and time course are absent in $\Delta F(t)/F$ traces of the nonfunctional indicator SR101. $\Delta F(t)/F$ scale bar in (E) also applies to (B)–(D). ROIs were sorted by x coordinate. (C) OGB-1-AM $\Delta F(t)/F$ traces over the interval indicated in (B) by dashed lines. Flares are marked blue and are interleaved in time with sparkles (red) and bursts (green). Scale bar: 50 s. (D) Image frames of OGB-1-AM $\Delta F(t)/F$ increases relative to movement onset during the first flare in (C) illustrating the broad spatial extent of flares. Scale bar: 100 μm. (E) Images from a 3D recording of $\Delta F(t)/F$ increases during a flare. Indicated depth values were measured relative to the pial surface.

(Charles et al., 1991; Chen et al., 1999), as assessed by imaging neuronal Ca^{2+} activity in Purkinje cell dendrites and molecular layer interneurons (data not shown). Thus, we found no support for the idea that flares were mechanically induced and proceeded to characterize flares in more detail (Table S3).

Among flares' interesting properties was their mode of initiation. Flares did not seem to involve a stereotyped manner of propagation, but usually arose similarly across multiple locomotor events within individual fields of view (n = 187 running bouts, 15 mice). At flare onset we typically saw a smaller number of fibers within the palisades exhibiting Ca^{2+} increases that resembled sparkles (Movie S2). Adjoining areas between palisade fibers also underwent Ca^{2+} activation. The number of sparkling fibers rose over 4.2 ± 1.4 s (range, 1.2 – 8.2 s; n = 93 events, 15 mice) until reaching peak activation (Figure 5D).

We initially wondered if isolated sparkles might be spontaneously occurring, "miniature" flares, perhaps analogous to the miniature postsynaptic potentials that represent spontaneous neurotransmission. Flares showed a similar pharmacological profile as sparkles and were eliminated by TTX (n = 44 running bouts, 5 mice) or γDGG (n = 45 running bouts, 4 mice) (Figure 6A and 6B) even while locomotor activity persisted. In isoflurane-anesthetized mice we never saw flares (14 recordings, 4 mice), even if we moved or electrically stimulated the animals' limbs (n = 13 stimulations, 3 mice; Figure S5). PPADS did not significantly affect flares (n = 20 running bouts, 3 mice; Figures 6A and 6B and Table S3). However, by comparing the SR101 and OGB-1-AM data channels we saw that Ca^{2+} increases during flares always occurred both in the palisades and the surrounding areas where finer Bergmann glial fibers lie (Figures 5D and 5E). This does not eliminate the possibility that flares might be seeded by or partly composed of sparkles, but does show that flares are not simply composites of multiple sparkles (Discussion).

We next characterized the spatial magnitude of flares, because events involving widespread activation might be more likely to have a role in animal behavior or large-scale brain dynamics. 3D imaging showed flares occurred over at least ~0.5 × 0.5 × 0.1 mm^3 (our maximum sample volume), reached significant depths of the molecular layer, and activated palisade fibers along large portions of their axial extent (Figure 5E), as compared to sparkles that had more limited axial size. Flares tapered dramatically toward the Purkinje cell layer, but sometimes involved and spread between a few Bergmann glial cell bodies. Thus, flares are macroscopic and cover several cerebellar microzones, divisions of the cerebellar cortex that map to parts of the body (Apps and Garwicz, 2005).

Ca^{2+} Flares Have Refractory Dynamics that Depend on Running History

As an initial investigation of flares' potential relevance to locomotor behavior, we analyzed the temporal relationships between the two. We found a consistent order of events and a refractory character to flares' occurrences.

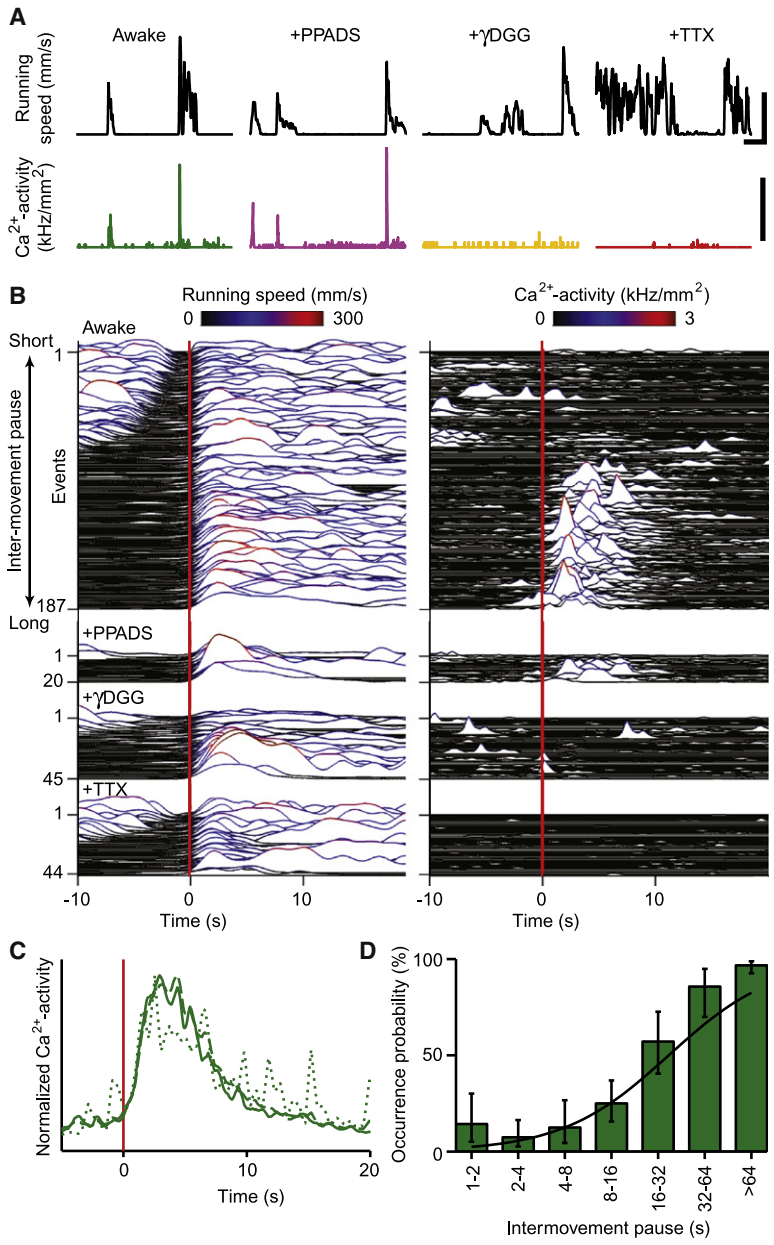

Figure 6. Locomotor-Evoked Ca^{2+} Flares Depend on Neuronal Activity, Have Limited Duration, and Exhibit a Refractory Period

(A) Example traces revealing Ca^{2+} flares (bottom) as a function of locomotor activity (black), under four conditions: awake-untreated (green; averaged signal from 194 ROIs), PPADS–treated (purple; 231 ROIs), γDGG–treated (orange; 192 ROIs), and TTX-treated (red; 191 ROIs). Data for each drug condition are from a different individual mouse. Concerted Ca^{2+} activity was quantified by the rate of palisade fiber activation per unit area using a threshold criterion of 10% $\Delta F(t)/F$ for each individual fiber. Scale bars: upper, 50 s and 150 mm/s; lower, 1 kHz/mm^2.

(B) Population data showing paired traces of running speed (left) and concurrent Ca^{2+} activity (right) in untreated (n = 187, 15 mice), PPADS-treated (n = 20, 3 mice), γDGG-treated (n = 45, 4 mice), and TTX-treated (n = 44, 5 mice) mice. Red lines indicate movement onset. For each condition, traces are ordered by the pause duration after the prior movement.

(C) Normalized mean time courses of flare activation triggered on movement onset (red line), for all (solid), brief (dotted), and extended movements (dashed), showing that flares have limited duration. Flares in (B) with peak amplitudes of at least 20 Hz/mm^2 were included for averaging.

(D) The probability of observing a flare at locomotor initiation versus the pause duration between movements, computed across the 187 movements shown in (B), showing that flares have a refractory period (compare to [B]). Error bars show 68% confidence intervals. Black curve represents a logistic regression.

Flares were refractory in that they arose more reliably at motor onset when there had been no prior recent movement. Thus, flares tended to accompany the initial but not the later movements within series of running bouts occurring in quick succession (Figure 6B). The percentage of cases in which flares occurred at motor onset rose from ~10% when the animal had moved in the previous 4 s (n = 27, 15 mice) to over ~86% if >32 s had elapsed since termination of the prior movement (n = 14, 15 mice) (Figure 6D). Only in 6.9% ± 5.9% (mean ± 68% confidence interval; n = 87, 15 mice) of cases did flares of significant extent and sparkling rates (>100 Hz/mm^2) occur without measurable rotation of the exercise ball, as assessed using the optical encoder.

Flares' peak activity always occurred after movement of the exercise ball and never before (Figures 6B–6D). Flares also had limited duration, regardless of how long the mouse's locomotor episode lasted (Figure 6C). If >10 s had elapsed since termination of the prior locomotor episode, flares reached peak fluorescence 4.4 ± 2.5 s after reinitiation of movement (n = 93 events, 15 mice) (Figure 6C). Ca^{2+} increases during flares persisted for 9.7 ± 2.8 s (n = 93 events, 15 mice) (Figure 6C). Thus, if locomotion was brief (<4 s) flares outlasted the movement, but vice versa if motor activity persisted (>16 s).

Kinetic Relationships of Flares to Motor Behavior and Hemodynamics

Prior work in vitro and in anesthetized animals has shown the involvement of astrocytic Ca^{2+} signaling in hemodynamic modulation (Iadecola and Nedergaard, 2007; Nimmerjahn, 2009). This suggests a possible link between flares and blood flow regulation. Thus, we quantified the kinetic relationships between locomotion, hemodynamics, and flares to logically constrain the roles flares might play (Tables S3 and S4).

Timescales of cerebral hemodynamic responses have been well reported (Huettel and McCarthy, 2000; Martin et al., 2006; Martindale et al., 2005), but we verified the basic kinetics of responses that occur in our mouse locomotor assay by using laser Doppler measurements of blood perfusion levels in the vermis (Table S4), and we compared these kinetics to those of flares (Figure 7). Local blood perfusion levels rose (median amplitude ± SD, 31% ± 11%; range, 16%–68%; n = 134 events, 11 mice) over a very similar time course as that of Ca^{2+} flares (Figure 7C).

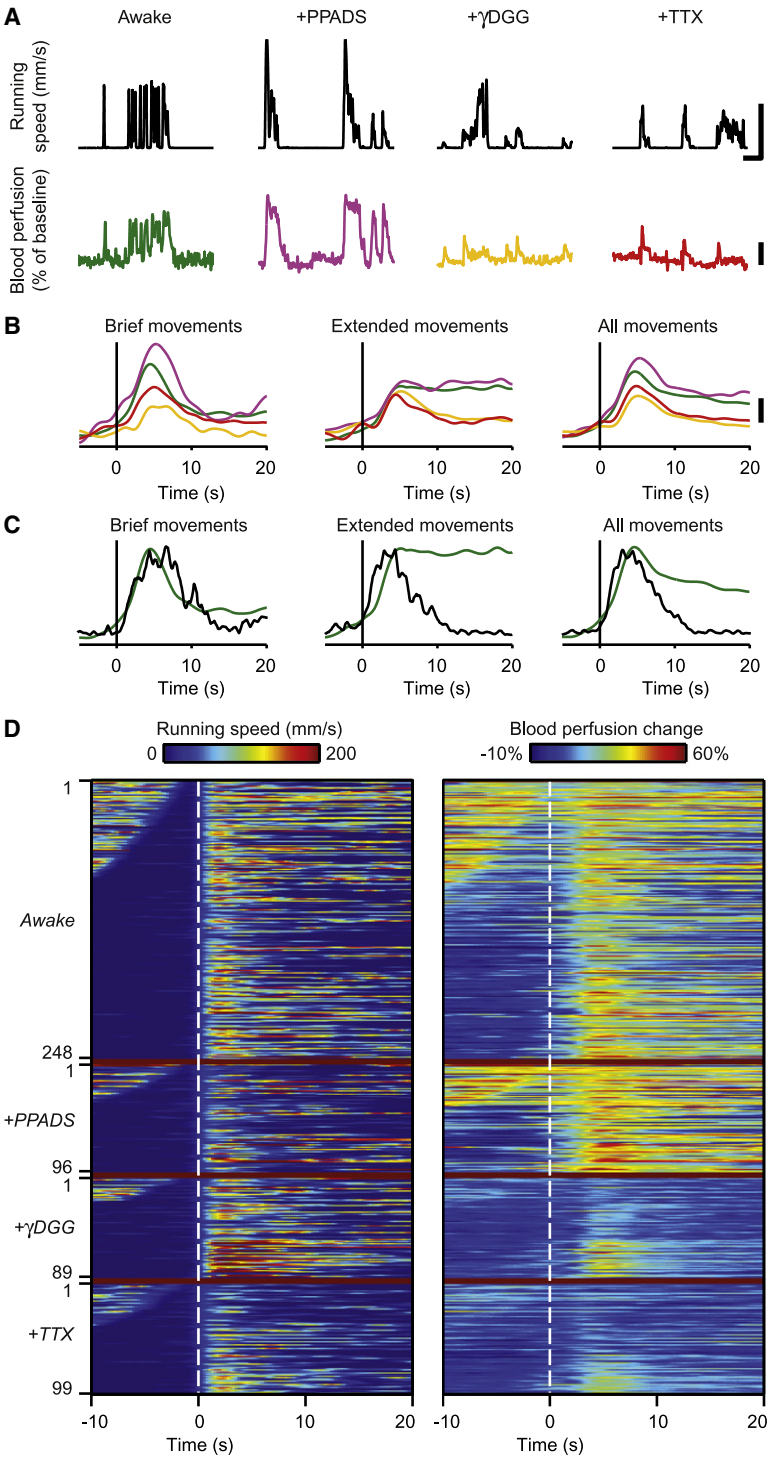

Figure 7. Temporal Relationships of Ca^{2+} Flares to Locomotor-Evoked Blood Perfusion Increases

(A) Example traces showing blood perfusion increases (bottom) as a function of locomotor activity (top), under four conditions: awake-untreated (green), PPADS-treated (purple), γDGG-treated (orange), and TTX-treated (red). Data for each drug condition are from a different individual mouse. Scale bars: upper, 50 s and 150 mm/s; lower, 20%.

(B) Population data showing overlay of average blood perfusion increases in untreated (green; n = 76, 11 mice), PPADS-treated (purple; n = 22, 2 mice), γDGG-treated (orange; n = 42, 4 mice), and TTX-treated (red; n = 28, 3 mice) mice triggered upon movement onset for brief (left), extended (center), and all movements (right). Traces from each trial were normalized by the peak running speed in that trial, prior to averaging. Note that TTX and γDGG reduce the amplitude of blood perfusion increases and reduce their persistence during extended running periods. Scale bar, 10%. Traces are based on a set of running bouts with > 100 mm/s peak running speed and an intermovement interval >15s.

(C) Overlay of average Ca^{2+} flare activation (black) and blood perfusion increase (green), triggered on movement onset (vertical lines), reveals similar kinetics during locomotor initiation in the untreated condition. Flares are not sustained during extended movements, but blood perfusion increases are. Flare traces are based on a set of 187 running bouts with peak running speeds >100 mm/s in 15 mice.

(D) Sets of paired traces of running speed (left) and corresponding blood perfusion increases (right) in untreated (n = 248, 11 mice), PPADS-treated (n = 96, 3 mice), γDGG-treated (n = 89, 4 mice), and TTX-treated mice (n = 99, 3 mice). Dashed lines indicate movement onset. For each condition, traces are ordered by the pause duration after the prior movement. TTX and γDGG particularly reduce the persistence of perfusion increases.

However, perfusion levels did not follow time courses similar to those of flares throughout locomotion (Figures 7C and 7D). Instead, hemodynamic upregulation persisted throughout motor behavior (median duration ± SD, 13 ± 36 s; range, 1.2–226 s; n = 134 events, 11 mice) (Figure 7D), as documented for other types of movement (Logothetis and Wandell, 2004). This persistence of blood flow responses contrasts with flares' limited duration (Figures 6B and 6C).

We also examined how the regulation of blood perfusion levels depended on neural activity and ATP-mediated signaling. Surface application to the vermis of either TTX or γDGG, but not PPADS, reduced the persistence of blood perfusion increases during extended periods of movement (Figure 7). Thus, the duration of blood flow responses was shortened by both TTX (6.1 ± 6.7 s, median ± SD; range, 1.4 – 27 s; n = 35 events, 3 mice; Wilcoxon rank sum test, $p < 10^{-4}$) and γDGG (7.2 ± 6.2 s, median ± SD; range, 1.1–27 s; n = 45 events, 4 mice; Wilcoxon rank sum test, $p < 10^{-5}$), but not PPADS (16 ± 22 s, median ± SD; range, 1.8–87 s; n = 47 events, 3 mice; Wilcoxon rank sum test, p = 0.18). The peak amplitudes of blood perfusion increases were also reduced by both TTX (median amplitude, 21% ± 4.9%; range, 15%–31%; n = 35 events, 3 mice; Wilcoxon rank sum test, $p < 10^{-9}$) and γDGG (median amplitude, 23% ± 8.5%; range, 15%–49%; n = 45 events, 4 mice; Wilcoxon rank sum test, $p < 10^{-5}$) but not PPADS (median amplitude, 42% ± 12%; range, 19%–60%; n = 47 events, 3 mice; Wilcoxon rank sum test,

p = 0.005). Taken together, the kinetic and pharmacological data (summarized in Table S4) suggest a potentially intricate relationship between flares, blood flow, and animal behavior (Discussion).

DISCUSSION

We conducted the initial study of Bergmann glial Ca^{2+} excitation in awake, behaving animals and found three types of Ca^{2+} excitation: flares, bursts, and sparkles. Bursts and sparkles are ongoing in awake animals at rest, whereas flares are macroscopic events that initiate during locomotor behavior with similar rise times as blood perfusion levels. The modes of initiation and pharmacological data suggest that sparkles and flares could share some common mechanisms distinct from those of bursts. Bursts require purinergic signaling but neither Na^+ channel activation nor glutamatergic transmission. In contrast, sparkles and flares are affected by blockade of either Na^+ channels or glutamatergic transmission, but not of purinergic signaling, and also by isoflurane anesthesia.

Isoflurane Anesthesia Disrupts Bergmann Glial Ca^{2+} Excitation

Recent studies have explored Ca^{2+} excitation in astrocytes of anesthetized animals (reviewed in Nimmerjahn, 2009). Comparison of our recordings from awake mice to those from the same fields of view while the mice were under isoflurane anesthesia provides reason to be cautious in interpreting results on astrocytic dynamics from anesthetized subjects. Isoflurane exerts direct and indirect effects on astrocytes, influencing glutamate uptake and gap-junction-mediated signaling (Mantz et al., 1993; Miyazaki et al., 1997). We found that isoflurane disrupts Bergmann glial Ca^{2+} excitation by eliminating flares and reducing sparkle rates, consistent with our other data suggesting that sparkles and flares are each promoted by neural activity. Interestingly, isoflurane reduced the estimated rate of sparkles even more than TTX or γDGG (Table S1), indicating that isoflurane might diminish both the intrinsic and the neuronal activity-dependent subpopulations of sparkles. Hence, wakefulness and animal behavior seem to be key influences on the excitation of glial networks.

Ca^{2+} Excitation Differs in Bergmann Glia and Protoplasmic Astrocytes

Studies in anesthetized animals have found spontaneous and sensory-evoked Ca^{2+} transients in protoplasmic astrocytes of the neocortex. The spontaneous transients were temporally sparse and arose in both individual astrocytic processes and cell bodies (Hirase et al., 2004; Takata and Hirase, 2008), although Ca^{2+} activity was reported to be more frequent in astrocyte processes than in cell bodies (Wang et al., 2006). Sensory-evoked Ca^{2+} transients were also restricted to individual astrocytes (Schummers et al., 2008; Wang et al., 2006) and required glutamatergic transmission (Petzold et al., 2008; Wang et al., 2006). Spontaneous transients were largely unaffected by TTX and PPADS (Takata and Hirase, 2008). In contrast, we found that Bergmann glia fibers show both highly localized and two forms of spreading Ca^{2+} transients. Spontaneously occurring bursts depended on purinergic signaling. Spontaneous Ca^{2+} excitation in Bergmann glial somata was rare, although sometimes Ca^{2+} excitation did spread among several Bergmann glial cell bodies during flares.

A recent study in the neocortical S1 hindlimb area of awake mice reported subpopulations of astrocytes that show Ca^{2+} activity correlated with running behavior (Dombeck et al., 2007). These Ca^{2+} increases lasted several seconds, and arose ~1–2 s after running onset. In comparison, locomotor-evoked cerebellar flares had no analogs in anesthetized mice, and displayed variable onset delays following running onset and relatively consistent durations. Whereas only a subpopulation of astrocytes in the S1 hindlimb area showed strong correlations with running behavior (Dombeck et al., 2007), running-evoked flares reliably involved hundreds of Bergmann glial fibers (Figure 5), except during the refractory period immediately following a prior movement (Figure 6). No refractory period was reported for neocortical astrocytes.

These differences in Ca^{2+} dynamics between star-shaped neocortical astrocytes and radially shaped Bergmann glia might be at least in part due to the distinct cellular organization and functional properties of these astrocytic cell types (Fiacco and McCarthy, 2006). Overall, our results highlight the need to compare astrocytic physiology across brain regions, between astrocytic subtypes, and under anesthesia to that appearing during animal behavior. Our results also show the utility of 3D imaging, which allowed us to reconstruct burst volumes and assess the axial extents of sparkles and flares. Comparisons of 3D data between different areas and layers will help reveal the diversities of roles astrocytes might play in brain dynamics.

Possible Causes of Sparkles

In vitro studies have shown that Bergmann glia can respond to neuronal activity with intracellular Ca^{2+} transients and that Ca^{2+} signaling plays a key role in regulating structural and functional interactions between these cells and cerebellar neurons (Iino et al., 2001). It has been unclear if these responses evoked in vitro have analogs in vivo. We found that Bergmann glia exhibit at least two types of spontaneous Ca^{2+} excitation. One of these types, sparkles, is highly localized and thus could be involved in synaptic function. We definitively identified sparkles within the palisade fibers, but our resolution in tissue bulk-loaded with OGB-1-AM does not permit us to judge whether the finer glial fibers closely adjacent to the palisades also undergo Ca^{2+} excitation during sparkles. Nor can we exclude a possible role for neuronal processes, particularly those that are closely entwined with the fine Bergmann glial processes. The sparkles detected within individual palisade fibers might be the result of intracellular Ca^{2+} waves that have initiated at microdomains in fine processes in nearby synapses and have then propagated to reach the main Bergmann glial fibers (Grosche et al., 1999). The low rate of sparkles we report is comparable to rates of spontaneous Ca^{2+} activity seen in vivo in neocortical astrocytes (Hirase et al., 2004; Takata and Hirase, 2008). Due to our conservative detection threshold, our sparkle rate estimate should be understood as a lower bound.

Since sparkles persist at reduced rates under TTX, γDGG, and isoflurane, sparkles could partly be of intrinsic origin, as are

spontaneous Ca^{2+} transients in neocortical astrocytes (Takata and Hirase, 2008). During locomotor activity, Ca^{2+} excitation due to flares arose across large numbers of palisade fibers, preventing us from making clear distinctions between isolated, individual sparkles and the widespread sparkle-like activity from the flares. Thus, it remains unclear whether there is a connection between sparkles and motor behavior.

Possible Causes of Bursts

Radially expanding bursts spread across the main glial fibers of the palisades as well as surrounding nonpalisade regions in the cerebellar molecular layer where fine Bergmann glial fibers lie, as reported also in a recent study (Hoogland et al., 2009). Were a neuronal role to exist in bursts, it should be independent of Na^+-channel-mediated voltage depolarization and glutamatergic transmission, since bursts persist under TTX and γDGG.

Bursts propagated outward from a central initiation site, which in some cases appeared to be an individual palisade fiber, with an approximate speed (~10 μm/s) comparable to reported speeds of intercellular Ca^{2+} waves seen in vitro in astrocytes of several types (Fiacco and McCarthy, 2006). Based on the size of bursts' radial expansion, bursts typically cover fibers from ~10 but sometimes up to a few tens of Bergmann glia. Using 3D imaging we found bursts spread over an approximately ellipsoidal volume of ~86,000 μm^3, yielding estimates that bursts traverse 55,000–70,000 parallel fiber-Purkinje cell synapses from approximately three adjoining Purkinje cells (Heinsen and Heinsen, 1983; Napper and Harvey, 1988). The 3D radially expanding waveform of bursts and the outward propagation of Ca^{2+} excitation suggest that a diffusible messenger could mediate bursts. Bursts' ellipsoidal volumes suggest that the diffusion of any such messenger is anisotropic, which is plausible given the ordered, anisotropic architecture of cerebellar cortex. ATP is a likely candidate as a messenger, since blockade of P2 purinergic receptors eliminates bursts. However, since extracellular hydrolysis of ATP likely occurs within ~200 ms of release (Dunwiddie et al., 1997), ATP is probably not involved in bursts' termination given that bursts last ~4–5 s.

The time course of bursts was well fit by a two-stage kinetic model and closely resembles that of large-amplitude Ca^{2+} transients evoked in Bergmann glia upon parallel fiber stimulation in brain slices (Beierlein and Regehr, 2006; Piet and Jahr, 2007). These evoked transients also involved purinergic receptor activation and release of Ca^{2+} from intracellular stores. Given these similarities, we interpret the ongoing bursts we saw in vivo as the physiological analogs of the evoked transients recorded in vitro. Electrical stimulation of parallel fibers in vitro may be one means of eliciting sufficient ATP release to trigger bursts. However, based on the persistence of bursts in vivo in the presence of TTX and γDGG, parallel fiber activity may not be the normal physiological means of triggering the ATP release that leads to bursts.

Although γDGG did not significantly alter the frequency of bursts, it did lengthen bursts' duration by reducing the rate constant k_2 in our kinetic model of two reaction steps. Thus, although glutamate transmission is not required for burst initiation, blockade of glutamate transmission does affect the termination of bursts. In vitro, blockade of AMPA glutamate receptors did not eliminate electrically evoked bursts, but did eradicate an initial component of the $[Ca^{2+}]$ increase in Bergmann glia that was small compared to the component sensitive to PPADS (Piet and Jahr, 2007). However, the available data do not permit us to make more precise conclusions about what glutamate's specific role might be (Supplemental Discussion).

Evidence implicating a specific function for bursts remains lacking. In thalamus, ATP release from astrocytes during astrocytic Ca^{2+} waves leads to a partial suppression of glutamatergic neurotransmission that is mediated by the ATP hydrolysis product adenosine (Bekar et al., 2008). By analogy, cerebellar Ca^{2+} bursts might also affect neurotransmission via adenosine signaling. However, in vitro studies have not found any influence of electrically evoked bursts upon parallel fiber to Purkinje cell synaptic transmission (Beierlein and Regehr, 2006). We saw considerable variability in burst rates between individual mice, and future work must identify the origins of this variability and the role of bursts in brain function. To date, we have not found any connection between bursts and locomotor activity.

Possible Causes of Flares

Ca^{2+} flares arose upon initiation of locomotor activity and often covered our entire field of view of 200–500 μm. At their initiation flares appear to be composed of multiple sparkles, combined with Ca^{2+} excitation in regions between the palisade fibers. Based on this appearance and the similar pharmacological sensitivities of flares and sparkles, it is tempting to speculate that sparkles could be seed or miniature flares. This speculation must be tempered on several grounds. Sparkles occur in animals at rest and persist at low rates under TTX or isoflurane, whereas the neural activity patterns needed to initiate flares in the areas we studied seem specific to motor behavior. Further, flares are more than just a composite of many sparkles, since flares activate both the main glial fibers in palisades and surrounding fine fibers. Our recordings do not have the resolution to eliminate the possibility that sparkles activate fine fibers closely adjacent to the palisades, but the data show conclusively the much tighter spatial association between sparkles and palisade fibers than for flares and palisade fibers.

Regardless of whether sparkles are precisely limited to the palisades, it is reasonable to hypothesize that a smaller number of localized events, such as sparkles, might together initiate a composite macroscopic event, a flare. This hypothesis prompts many questions for future study, including, "How many palisade fibers must undergo Ca^{2+} activation to achieve a flare, and under what conditions can this collective event occur?" An interesting aspect of flares is their refractory period of ~30 s (Figure 6D). Given that Ca^{2+} excitation in astrocytes is thought to occur primarily through release of Ca^{2+} from intracellular stores (Fiacco and McCarthy, 2006), the refractory duration may correspond to the time needed to replenish these stores following Ca^{2+} depletion. Overall, network Ca^{2+} activation during flares contrasts with that of bursts, which appear to have a single initiation site, use different receptor pathways, and cover only tens of cells.

As with sparkles and bursts, although we can definitively state the involvement of Bergmann glial palisade fibers in flares, we cannot exclude a possible role for neurons in flares in regions

outside the palisade fibers. On the contrary, in the scenario that flares mediate signals between neurons and blood vessels, neurons would clearly have a key role in flares' initiation.

Possible Relationships of Flares to Motor Behavior and Hemodynamics

Given their size and behaviorally triggered character, flares seem well poised to influence neuronal or cerebral blood flow dynamics associated with motor behavior. Recent research has paid considerable attention to the potential role of astrocytes in functional hyperemia, the upregulation of cerebral blood flow in response to heightened neural activity (Iadecola and Nedergaard, 2007). Like other cortical astrocytes Bergmann glia contact neuronal synapses and blood vessels. Hence, flares might help mediate locomotor-driven blood flow increases. Our kinetic and pharmacological data are consistent with a possible role for Bergmann glial Ca^{2+} flares in blood flow responses, but do not conclusively prove a connection between the two phenomena. In the vermis, flares and blood perfusion responses arise over similar time courses following locomotor initiation and are both reduced by TTX and γDGG, but not PPADS. Notable differences are that flares have a refractory period and a limited duration, whereas blood perfusion responses are not refractory and persist throughout locomotor activity. TTX and γDGG, which block flares, preferentially reduce the persistence of blood flow responses. It is also well established that cerebellar blood flow responses can be evoked in anesthetized animals (Yang et al., 2000), whereas flares were absent under isoflurane anesthesia (Table S3 and Figure S5).

These data are consistent with a number of plausible scenarios in which flares occur in direct response to the neural activity underlying locomotion and mediate changes in blood flow. Complications in considering these possibilities are that for technical reasons our imaging and laser Doppler studies used separate sets of animals, and that the ~1 mm depth of tissue sampled by our laser Doppler measurements was greater than the ~200 μm tissue depths sampled in our two-photon imaging studies. Thus, the failure of TTX and γDGG to abolish blood flow responses entirely could be due to incomplete effects of the drugs on the deeper tissues sampled in the blood perfusion studies. Prior laser Doppler studies in anesthetized animals have also found that functional hyperemia in the cerebellum is only partially reduced by surface application of TTX or glutamate antagonists (Iadecola et al., 1996; Yang and Iadecola, 1998).

One scenario consistent with our data is that flares help mediate the persistence, but not the initial rise, of blood flow responses. Elimination of flares by TTX or γDGG would thus lead to the preferential decline in persistent blood perfusion responses that we observed (Figure 7). However, an additional signaling mechanism would be needed to explain how blood flow responses are maintained over the duration of longer movements and then terminated. This other signal could either maintain persistent blood flow responses over the duration of motor activity, or mediate the termination of blood flow responses. Combinations of these alternatives are also possible.

In another plausible scenario, the similarity in the rise times of flares and blood flow upregulation is due to a direct role for flares in the initiation of blood flow responses. In this case, persistent blood flow responses would be initiated and maintained by other signals, such as direct signals sent from neurons to blood vessels. In anesthetized animals it has been shown that the activity of cerebellar molecular layer interneurons triggers blood flow responses via release of nitric oxide (NO) (Yang et al., 1999, 2000). Since flares are not of sufficient duration to have a role in the maintenance of blood flow responses during extended periods of neural activity (Figure 6), NO signals from interneurons might have this maintenance role.

In contrast to the two scenarios just considered in which flares influence blood flow, another conceivable possibility is that increases in blood flow, rather than increases in neural activity, trigger flares. In this case, flares might provide retrograde signaling from blood vessels to neuropil (Moore and Cao, 2008), although there is presently less data to support such a possibility. It is also conceivable that flares are part of a dynamical interplay between neurons and astrocytes that mediates animal behavior. For example, flares might cause Bergmann glia to release neuroactive molecules, in turn affecting the neural activity underlying locomotion. Other possibilities involve combinations of such scenarios. To dissect these issues, microscopy in behaving mice must be combined with cell-type-specific manipulations, such as by genetic or optogenetic means.

EXPERIMENTAL PROCEDURES

Animals and Surgery

All procedures were approved by the Stanford APLAC. We used male C57BL/6 mice (6–10 weeks old). Surgery was done under isoflurane (1.5%–2.5%, mixed with 1–2 l/min O_2). One to two weeks prior to imaging, the skull was exposed and cleaned above neocortex and cerebellum. A custom metal plate allowing cranial access and repeated head fixation was fixed to the skull with dental acrylic (Coltene/Whaledent, H00335).

On the imaging day, a craniotomy (0.5–3.5 mm diameter) was opened (−6.5 mm posterior to bregma; 0.5 mm lateral). Exposed tissue was irrigated with warm artificial cerebral spinal fluid (ACSF; 125 mM NaCl, 5 mM KCl, 10 mM D-Glucose, 10 mM HEPES, 2 mM $CaCl_2$, 2 mM $MgSO_4$; pH to 7.4 with NaOH). To dampen heartbeat- and breathing-induced brain motion, the craniotomy was filled with agarose (1.5%; Type III-A, high EEO; Sigma) in ACSF and covered by a coverslip fixed to the head plate, creating an optical window. The dura was left intact for Ca^{2+} indicator injections and control experiments regarding mechanical stress, but generally removed just prior to agarose application to allow pharmacological interventions and electrical recordings. In some cases Teflon-coated silver wires (A-M Systems, 785500 and 787000) were implanted for electro-corticogram (ECoG) recordings.

Indicator Labeling

Targeted bulk-loading of cerebellar tissue with the Ca^{2+} indicator OGB-1-AM (Molecular Probes) was done as described (Stosiek et al., 2003). Concentrations of OGB-1-AM and DMSO in our pipette solution were 500 μM and 2%–5%, respectively. To counterstain Bergmann glia, the red fluorescent astrocyte marker SR101 (200–333 μM in ACSF; Invitrogen) was added to the injection solution or applied topically (1–5 min) in cases in which the dura was removed (Nimmerjahn et al., 2004).

Imaging

After surgical implantation of the head plate and a recovery of 1–7 days, mice were habituated in 3–10 sessions (usually 1 session/day) to accept increasingly longer periods (15–135 min sessions; 2.5–9.25 hr total habituation time) of head restraint while on a 11.9 cm diameter exercise ball (Habitrail, 62065) covered with copper mesh. The ball rotated on one axis, allowing the animal to stride forward or backward at liberty.

We used a custom upright two-photon microscope equipped with an ultrafast Ti:sapphire laser (Tsunami, Spectra-Physics), a nanofocusing system (P-725-PIFOC, Physik Instrumente), two detection channels, and a 20 × water-immersion objective (Olympus, 0.95 NA, XLUMPlanFI). For simultaneous excitation of OGB-1-AM and SR101, we ordinarily used 800–820 nm. To minimize aftereffects of anesthesia, mice recovered from isoflurane for >60 min prior to recordings. To minimize the possibility of photo-induced alterations in physiology, the duration and average power of continuous illumination typically were <7 min and <35 mW at a given brain location.

Images were typically 256 × 256 pixels (10.2–11.1 Hz frame rate) or 128 × 128 pixels (20.4 Hz), but sometimes 512 × 512 pixels (2 Hz frame rate) to obtain higher resolution. In 3D recordings, image stacks contained 5–20 optical sections acquired at 5, 10, or 20 μm axial spacing (1–4 Hz stack acquisition rate).

Behavioral Analysis

Rotations of the exercise ball were monitored using an optical encoder (US Digital, E7PD-720-118). In addition, mouse behavior was recorded in Mini-DV format using a digital camcorder (Sony DCR-VX2000).

Electrophysiology

For ECoG recording the stripped tip of a 140-μm-diameter Teflon-coated silver wire (A-M Systems, 785500) was placed on the pial surface in one corner of the craniotomy. A 330-μm-diameter reference electrode (A-M Systems, 787000) was placed over neocortex near bregma through a small hole in the parietal bone. ECoG signals were acquired using a differential AC amplifier (A-M Systems, 1700; gain, 1000–10,000; Notch filtered).

Pharmacology

TTX (25–125 μM), γDGG (50 mM), and PPADS (1–2 mM) were dissolved in ACSF and applied in aqueous solution onto the optical window in the cranium. Drug action was generally verified by observing changes in ECoG recordings. For each drug treatment, we always performed within animal comparisons of Ca^{2+} transients occurring at the same field of view before and during the treatment. Since washout of drugs can be imperfect, we used a separate set of animals for each drug tested.

Laser Doppler Studies

We tracked blood perfusion levels using an instrument (PF-5010-LDPM, Perimed) with a 1 mm diameter fiber-optic probe (PR 407-1) that we affixed either to the cranium or to an optical window using a miniature probe holder (PH 07-6). A smoothing filter with a 0.03 s time constant was applied to all perfusion traces.

General Methods of Image Analysis

As a first analysis step, we corrected any lateral motion artifacts in the imaging data. We then corrected for photobleaching and for spectral overlap in the emission spectra of the two dyes. ROIs containing glial fiber palisades were identified in SR101 images by applying a spatial high-pass filter and then finding contiguous regions above a threshold intensity value. To obtain Ca^{2+} signals we examined the glial palisade ROIs within the OGB-1-AM images and extracted $\Delta F(t)/F$ traces for each ROI.

Statistical Analysis

Data analysis algorithms were written in MATLAB (Mathworks). All values reported in the text are mean ± SD, except those noted as median ± SD and the errors in event percentages and rates, which are 68% confidence intervals. See Supplemental Data for more details.

SUPPLEMENTAL DATA

The supplemental data for this article include Supplemental Experimental Procedures, Discussion, five figures, four tables, and two movie files and can be found at http://www.neuron.org/supplemental/S0896-6273(09)00244-X.

ACKNOWLEDGMENTS

We thank B.A. Barres, B. Stevens, and members of the Barres lab for helpful conversations and S100β-EGFP mice; D. Profitt and Stanford's Varian Machine Shop for expert machining; A. Lui for programming assistance and help with habituating animals; and Q.T. Nguyen and D. Kleinfeld for providing imaging software and electronics. Our work was supported by grants to M.J.S. from NIDCD, the NIH NDC for Optical Control of Biological Function, the Stanford Bio-X program, and the Klingenstein, Sloan, and Packard Foundations; postdoctoral fellowships to A.N. from the Alexander von Humboldt-Foundation and the International Human Frontier Science Program Organization; and an NSF Graduate Fellowship to E.A.M.

Accepted: March 9, 2009
Published: May 13, 2009

REFERENCES

Andersson, G., and Armstrong, D.M. (1987). Complex Spikes in Purkinje-Cells in the Lateral Vermis (B-Zone) of the Cat Cerebellum during Locomotion. J. Physiol. *385*, 107–134.

Apps, R., and Garwicz, M. (2005). Anatomical and physiological foundations of cerebellar information processing. Nat. Rev. Neurosci. *6*, 297–311.

Beierlein, M., and Regehr, W.G. (2006). Brief bursts of parallel fiber activity trigger calcium signals in Bergmann glia. J. Neurosci. *26*, 6958–6967.

Bekar, L., Libionka, W., Tian, G.F., Xu, Q., Torres, A., Wang, X., Lovatt, D., Williams, E., Takano, T., Schnermann, J., et al. (2008). Adenosine is crucial for deep brain stimulation-mediated attenuation of tremor. Nat. Med. *14*, 75–80.

Charles, A.C., Merrill, J.E., Dirksen, E.R., and Sanderson, M.J. (1991). Intercellular Signaling in Glial-Cells - Calcium Waves and Oscillations in Response to Mechanical Stimulation and Glutamate. Neuron *6*, 983–992.

Chen, G., Hanson, C.L., Dunbar, R.L., and Ebner, T.J. (1999). Novel form of spreading acidification and depression in the cerebellar cortex demonstrated by neutral red optical imaging. J. Neurophysiol. *81*, 1992–1998.

De Blas, A.L. (1984). Monoclonal-Antibodies to Specific Astroglial and Neuronal Antigens Reveal the Cytoarchitecture of the Bergmann Glia Fibers in the Cerebellum. J. Neurosci. *4*, 265–273.

Dombeck, D.A., Khabbaz, A.N., Collman, F., Adelman, T.L., and Tank, D.W. (2007). Imaging large-scale neural activity with cellular resolution in awake, mobile mice. Neuron *56*, 43–57.

Dunwiddie, T.V., Diao, L., and Proctor, W.R. (1997). Adenine nucleotides undergo rapid, quantitative conversion to adenosine in the extracellular space in rat hippocampus. J. Neurosci. *17*, 7673–7682.

Fiacco, T.A., and McCarthy, K.D. (2006). Astrocyte calcium elevations: Properties, propagation, and effects on brain signaling. Glia *54*, 676–690.

Gobel, W., Kampa, B.M., and Helmchen, F. (2007). Imaging cellular network dynamics in three dimensions using fast 3D laser scanning. Nat. Methods *4*, 73–79.

Greenberg, D.S., Houweling, A.R., and Kerr, J.N.D. (2008). Population imaging of ongoing neuronal activity in the visual cortex of awake rats. Nat. Neurosci. *11*, 749–751.

Grosche, J., Matyash, V., Moller, T., Verkhratsky, A., Reichenbach, A., and Kettenmann, H. (1999). Microdomains for neuron-glia interaction: parallel fiber signaling to Bergmann glial cells. Nat. Neurosci. *2*, 139–143.

Heinsen, H., and Heinsen, Y.L. (1983). Quantitative Studies on Regional Differences in Purkinje-Cell Dendritic Spines and Parallel Fiber Synaptic Density. Anat. Embryol. (Berl.) *168*, 361–370.

Hirase, H., Qian, L.F., Bartho, P., and Buzsaki, G. (2004). Calcium dynamics of cortical astrocytic networks in vivo. PLoS Biol. *2*, E96.

Hoogland, T.M., Kuhn, B., Gobel, W., Huang, W., Nakai, J., Helmchen, F., Flint, J., and Wang, S.S. (2009). Radially expanding transglial calcium waves in the intact cerebellum. Proc. Natl. Acad. Sci. USA *106*, 3496–3501.

Huettel, S.A., and McCarthy, G. (2000). Evidence for a refractory period in the hemodynamic response to visual stimuli as measured by MRI. Neuroimage *11*, 547–553.

Iadecola, C., and Nedergaard, M. (2007). Glial regulation of the cerebral microvasculature. Nat. Neurosci. *10*, 1369–1376.

Iadecola, C., Li, J., Xu, S., and Yang, G. (1996). Neural mechanisms of blood flow regulation during synaptic activity in cerebellar cortex. J. Neurophysiol. *75*, 940–950.

Iino, M., Goto, K., Kakegawa, W., Okado, H., Sudo, M., Ishiuchi, S., Miwa, A., Takayasu, Y., Saito, I., Tsuzuki, K., and Ozawa, S. (2001). Glia-synapse interaction through Ca2+-permeable AMPA receptors in Bergmann glia. Science *292*, 926–929.

Jorntell, H., Ekerot, C., Garwicz, M., and Luo, X.L. (2000). Functional organization of climbing fibre projection to the cerebellar anterior lobe of the rat. J. Physiol. *522*, 297–309.

Koekkoek, S.K.E., Den Ouden, W.L., Perry, G., Highstein, S.M., and De Zeeuw, C.I. (2002). Monitoring kinetic and frequency-domain properties of eyelid responses in mice with magnetic distance measurement technique. J. Neurophysiol. *88*, 2124–2133.

Leicht, R., and Schmidt, R.F. (1977). Somatotopic Studies on Vermal Cortex of Cerebellar Anterior Lobe or Unanesthetized Cats. Exp. Brain Res. *27*, 479–490.

Logothetis, N.K., and Wandell, B.A. (2004). Interpreting the BOLD signal. Annu. Rev. Physiol. *66*, 735–769.

Mantz, J., Cordier, J., and Giaume, C. (1993). Effects of General-Anesthetics on Intercellular Communications Mediated by Gap-Junctions between Astrocytes in Primary Culture. Anesthesiology *78*, 892–901.

Martin, C., Martindale, J., Berwick, J., and Mayhew, J. (2006). Investigating neural-hemodynamic coupling and the hemodynamic response function in the awake rat. Neuroimage *32*, 33–48.

Martindale, J., Berwick, J., Martin, C., Kong, Y.Z., Zheng, Y., and Mayhew, J.E.W. (2005). Long duration stimuli and nonlinearities in the neural-haemodynamic coupling. J. Cereb. Blood Flow Metab. *25*, 651–661.

Miyazaki, H., Nakamura, Y., Arai, T., and Kataoka, K. (1997). Increase of glutamate uptake in astrocytes - A possible mechanism of action of volatile anesthetics. Anesthesiology *86*, 1359–1366.

Moore, C.I., and Cao, R. (2008). The hemo-neural hypothesis: On the role of blood flow in information processing. J. Neurophysiol. *99*, 2035–2047.

Napper, R.M.A., and Harvey, R.J. (1988). Number of Parallel Fiber Synapses on an Individual Purkinje-Cell in the Cerebellum of the Rat. J. Comp. Neurol. *274*, 168–177.

Nett, W.J., Oloff, S.H., and McCarthy, K.D. (2002). Hippocampal astrocytes in situ exhibit calcium oscillations that occur independent of neuronal activity. J. Neurophysiol. *87*, 528–537.

Nimmerjahn, A. (2009). Astrocytes going live: advances and challenges. J. Physiol. *587*, 1639–1647.

Nimmerjahn, A., Kirchhoff, F., Kerr, J.N.D., and Helmchen, F. (2004). Sulforhodamine 101 as a specific marker of astroglia in the neocortex in vivo. Nat. Methods *1*, 31–37.

Petzold, G.C., Albeanu, D.F., Sato, T.F., and Murthy, V.N. (2008). Coupling of neural activity to blood flow in olfactory glomeruli is mediated by astrocytic pathways. Neuron *58*, 897–910.

Piet, R., and Jahr, C.E. (2007). Glutamatergic and purinergic receptor-mediated calcium transients in Bergmann glial cells. J. Neurosci. *27*, 4027–4035.

Reichenbach, A., Siegel, A., Rickmann, M., Wolff, J.R., Noone, D., and Robinson, S.R. (1995). Distribution of Bergmann Glial Somata and Processes - Implications for Function. J. Brain Res. *36*, 509–517.

Rinberg, D., Koulakov, A., and Gelperin, A. (2006). Sparse odor coding in awake behaving mice. J. Neurosci. *26*, 8857–8865.

Schummers, J., Yu, H.B., and Sur, M. (2008). Tuned responses of astrocytes and their influence on hemodynamic signals in the visual cortex. Science *320*, 1638–1643.

Shibuki, K., Gomi, H., Chen, L., Bao, S.W., Kim, J.S.K., Wakatsuki, H., Fujisaki, T., Fujimoto, J., Katoh, A., Ikeda, T., et al. (1996). Deficient cerebellar long-term depression, impaired eyeblink conditioning, and normal motor coordination in GFAP mutant mice. Neuron *16*, 587–599.

Stosiek, C., Garaschuk, O., Holthoff, K., and Konnerth, A. (2003). In vivo two-photon calcium imaging of neuronal networks. Proc. Natl. Acad. Sci. USA *100*, 7319–7324.

Takata, N., and Hirase, H. (2008). Cortical layer 1 and layer 2/3 astrocytes exhibit distinct calcium dynamics in vivo. PLoS ONE *3*, e2525.

Wang, X., Lou, N., Xu, Q., Tian, G.F., Peng, W.G., Han, X., Kang, J., Takano, T., and Nedergaard, M. (2006). Astrocytic Ca2+ signaling evoked by sensory stimulation in vivo. Nat. Neurosci. *9*, 816–823.

Yang, G., and Iadecola, C. (1998). Activation of cerebellar climbing fibers increases cerebellar blood flow: role of glutamate receptors, nitric oxide, and cGMP. Stroke *29*, 499–507.

Yang, G., Chen, G., Ebner, T.J., and Iadecola, C. (1999). Nitric oxide is the predominant mediator of cerebellar hyperemia during somatosensory activation in rats. Am. J. Physiol. *277*, R1760–R1770.

Yang, G., Huard, J.M.T., Beitz, A.J., Ross, M.E., and Iadecola, C. (2000). Stellate neurons mediate functional hyperemia in the cerebellar molecular layer. J. Neurosci. *20*, 6968–6973.

Zuo, Y., Lubischer, J.L., Kang, H., Tian, L., Mikesh, M., Marks, A., Scofield, V.L., Maika, S., Newman, C., Krieg, P., and Thompson, W.J. (2004). Fluorescent proteins expressed in mouse transgenic lines mark subsets of glia, neurons, macrophages, and dendritic cells for vital examination. J. Neurosci. *24*, 10999–11009.